

Supporting Information

Enhancing the Stability of Air-Processed Perovskite Solar Cells through a Self-Healing Polymer with Dynamic Molecular Locks for Grain Boundary Engineering

Juxiang Chen,[†] Jiangning Li,[†] Tian Wang, Qisong Yuan, Xiangrong Shi, Xin Li,* Bo Jiang*

School of Chemistry and Chemical Engineering, Harbin Institute of Technology, Harbin
150001, China

* Corresponding author: X. Li, B. Jiang.

[†] These authors contributed equally to this work.

E-mail: jiangbo5981@hit.edu.cn, lixin@hit.edu.cn

Experimental Section

1.1 Raw materials

The SnO₂ colloid solution (12 wt% in H₂O), bis(trifluoromethylsulfonyl)imide lithium (Li-TFSI), 2,2',7,7'-tetrakis(N,N-dimethoxyphenylamine)-9,9'-spirobifluorene(Spiro-OMeTAD), 4-tert-butylpyridine (t-BP) and were purchased from Xi'an Yuri Solar Co., Ltd. Bis(4-aminophenyl) disulfide (AFD), dibutyltin dilaurate (DBTDL), isophorone diisocyanate (IPDI), 4,4'-bis(hydroxymethyl)-2,2'-dipyridine (BHB), anhydrous tetrahydrofuran with molecular sieves (THF), dimethylsulfoxide (DMSO), dimethyl formamide (DMF), anhydrous acetonitrile with molecular sieve (ACN), and chlorobenzene were acquired from Energy Chemical (China). Bis(3-aminopropyl) terminated poly(dimethylsiloxane) (PDMS) were acquired from Gelest Inc. PbI₂, FAI, MABr, CsI, and fluorine-doped tin oxide (FTO) substrates were acquired from Youxuan Trading. All the reagents were commercially purchased without any purification furthermore.

1.2 Synthesis of self-healing polymer (PAB)

PDMS (18.000 g) was heated up to 100 °C for 30 min under vacuum to remove impurity, and cooled to ambient temperature. Next, the THF (65 mL) as solvent was added into the PDMS liquid. Then, the IPDI solution combined with IPDI (12 mmol, 2.667 g) and 20 mL THF was instilled into the performed polymer at 25 °C and stirred for 12 h in a protective gas (N₂) atmosphere of nitrogen. Afterwards the AFD (6 mmol, 1.298 g), BHB (6 mmol, 1.285 g) as chain extenders and two drops DBTDL catalyst were blended into 38 mL anhydrous THF and 4 mL anhydrous ACN, and instilled into the above reactants at 80 °C for 24 h in a protective gas atmosphere of nitrogen, respectively. Finally, The self-healing polymer was prepared after enriched and desiccate in 85 °C vacuum environment for 12 h.

1.3 Device Fabrication

All devices manufacturing processes are carried out in a fully open air. PSC devices were fabricated with the structure of fluorine-doped tin oxide (FTO)/SnO₂/Perovskite/Spiro-

OMeTAD/Au and PEN/FTO/SnO₂/perovskite/Spiro-OMeTAD/Au in open-air atmosphere. FTO and PEN were scrubbed and sonicated with detergent, water, acetone, and ethanol for 20 min in proper order. Then, FTO and PEN were treated with UV-ozone. A thin film of SnO₂ (4 wt%) was formed on both FTO and PEN surfaces through spin-coating (4000 rpm, 30 s), subsequently calcined at 150 °C in about 30 minutes. Following this step, the perovskite precursor solution was manufactured by blending FAI (224.4 mg), PbI₂ (742.2 mg), CsI (19.8 mg) and MABr (16.2 mg), in a commixture of dimethyl formamide and dimethylsulfoxide (volume ratio of 4:1). Before spin coating, introduce different amounts of PAB (5 mg•mL⁻¹ in tetrahydrofuran) with a molar ratio of 0.01%, 0.03%, 0.05%, 0.08%, 0.1% to perovskite (PVK). Then, the Spiro-OMeTAD commixture solution was a blend of 72.3 mg Spiro-OMeTAD, 1 mL chlorobenzene solution with 28.8 μL t-BP and 17.5 μL Li-TFSI (520 mg•mL⁻¹ in acetonitrile). Finally, thermal evaporation was employed to deposit the gold electrode, and the device's effective area was carefully controlled to 0.09 cm².

1.4 Films characterization

The thermostability of PAB was characterized by TA 2050, the sample was heated from 50 to 800 °C at a rate of 10 °C•min⁻¹ in a nitrogen atmosphere. The mechanical properties of PAB and PAB after self-healing were carried out on SANS (the maximum load 80 N), the tensile rate is 10 mm•min⁻¹. The surface morphology and granulometry of perovskite films were observed using a field emission scanning electron microscope (ZEISS SUPRA55, Germany) under 15 kV. The detection limit of EDS was generally 0.1%-0.5%, and the quantitative phase error of the main element without overlapping peak of medium atomic number was about 2%. The number of scanning repetitions was 3.

Multi-module scanning probe microscopy combined with atomic force microscopy was used to assess the microscopic morphology and Young's modulus of the perovskite films. (Dimension Fastscan, Germany). Optical contact angle meter (SL200KB, KINO Industry CO. Ltd., USA) was tested to observe the hydrophobic property of the polymer and perovskite

film surface. The crystal structure and crystallinity of the films were characterized by X-ray diffractometer (D8 ADVANCE, Bruker, Germany) with a Cu K α radiation. Rotation range was 0°-168°, radius of goniometer was ≥ 200 mm, scan step size was 0.001°, angle reproducibility was 0.001°, drive mode was stepper motor drive, maximum positioning speed was $\geq 1000^\circ/\text{mm}$. Using X-ray photoelectron spectroscopy (XPS) and fourier transform infrared spectroscopy (FTIR) were conducted to study the interaction between PAB and perovskite films. XPS analysis was conducted on a Thermo-VG Scientific ESCALAB 250 photoelectron spectrometer (Al K α) integrated with a MAGCIS ion gun, and the C1s peak was measured at 284.8 eV. The energy range utilized for the analysis extended from 100 eV to 4 keV. The maximum beam at 3 keV was greater than 6 μA . Minimum spot size was 200 μm at 2.5 μA and 4 keV. Analysis chamber Limit vacuum was 5×10^{-10} mbar. The Motion range of X axis and Y axis was 50 mm and 20 mm, resolution was 1 micron. Ranging from 300 μm to ~ 2.5 mm, the optical system provides a versatile field of view. The Sample tilt range of horizontal -90° to +60°. Fourier transform infrared spectroscopy (Nicolet IS50, Bruker, USA) was demonstrated by spectral resolution (0.09 cm^{-1}), spectral range (12000-50 cm^{-1}), wavenumber accuracy (0.005 cm^{-1}), slowest scanning speed (0.0063 cm/s), fastest scanning speed (8.86 cm/s).

Using a TU1901 spectrometer (Beijing Purkinje General Instrument Co., Ltd), the absorption and transmission properties of the perovskite films were assessed. Steady-state photoluminescence (PL) measurements were performed with an FLS980 spectrometer (Edinburgh Instruments). The electrostatic potential calculations were performed using the Gaussian16 software. The job type was set to geometry optimization followed by frequency analysis. The photovoltaic performance of the devices was evaluated under simulated AM1.5G solar irradiation (100 $\text{mW} \cdot \text{cm}^{-2}$) using an XES-100S1 solar simulator (Class AAA, San-EI Electric Co., Ltd.). A standard silicon solar cell was employed to calibrate the light

intensity of the solar simulator (1218, Newport, USA). The PCE was measured with a QTest Station 500D system (CROWNTECH, USA), which integrated a 300 W tungsten lamp, a QEM11-S 1/8 m monochromator, a Keithley 2000 multimeter, and an opaque chamber for precise quantum efficiency analysis. An electrochemical workstation was used to measure EIS, Capacitance-voltage (C-V) and SCLC curves (VersaSTAT 3, Ametek, USA). The photovoltaic performance of the control and doped PSCs was evaluated through J-V curve measurements under simulated AM 1.5G solar irradiation ($100 \text{ mW} \cdot \text{cm}^{-2}$).

Gaussian 16 was used to calculate the density universal function theory (DFT). All atoms were computed using the B3LYP functional with the LANL2DZ basis set for geometry optimization. Geometry optimization was performed initially, followed by frequency calculations to verify the absence of imaginary frequencies and the minimization of the potential energy surface.

Through parametric design language of ANSYS APDL, the finite element model of stress distribution in control and doped flexible films under stress bending state was established, and the nonlinear analysis was carried out to obtain the stress cloud diagram of control and doped flexible films under the action of mid-span concentrated load.

2. Figures and Tables

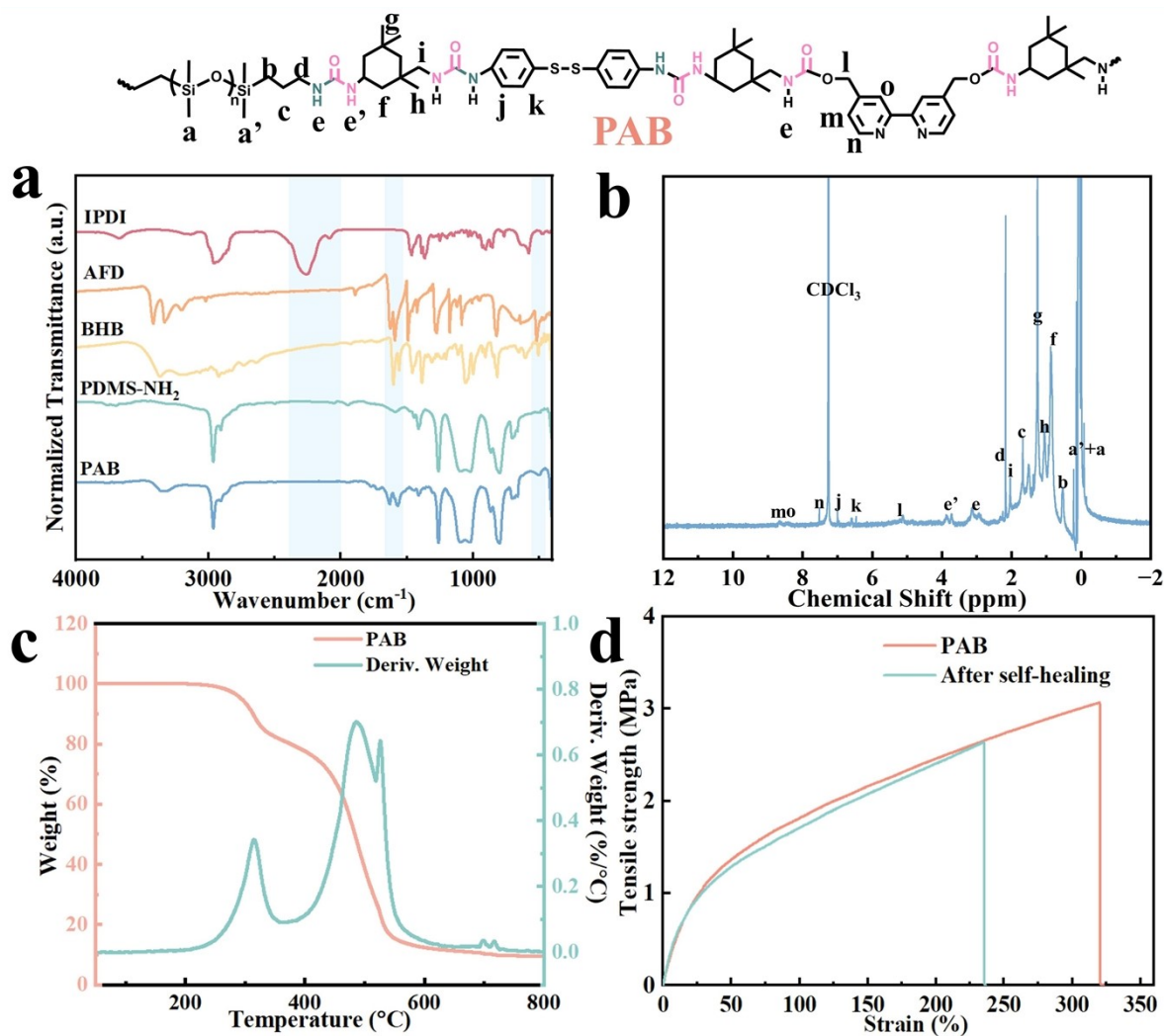


Fig. S1 (a) FT-IR spectra of IPDI, AFD, BHB, PDMS-NH₂, PAB. (b) ¹H NMR spectra of PAB. (c) The TG and DTG curves of PAB. (d) The stress-strain curves curves of PAB and after self-healed process at room temperature for 2 h. The polymer exhibited glorious mechanical strength (3.06 MPa) and tensile strain (320.11 %), and its mechanical properties could be restored to a certain extent after self-healed process.

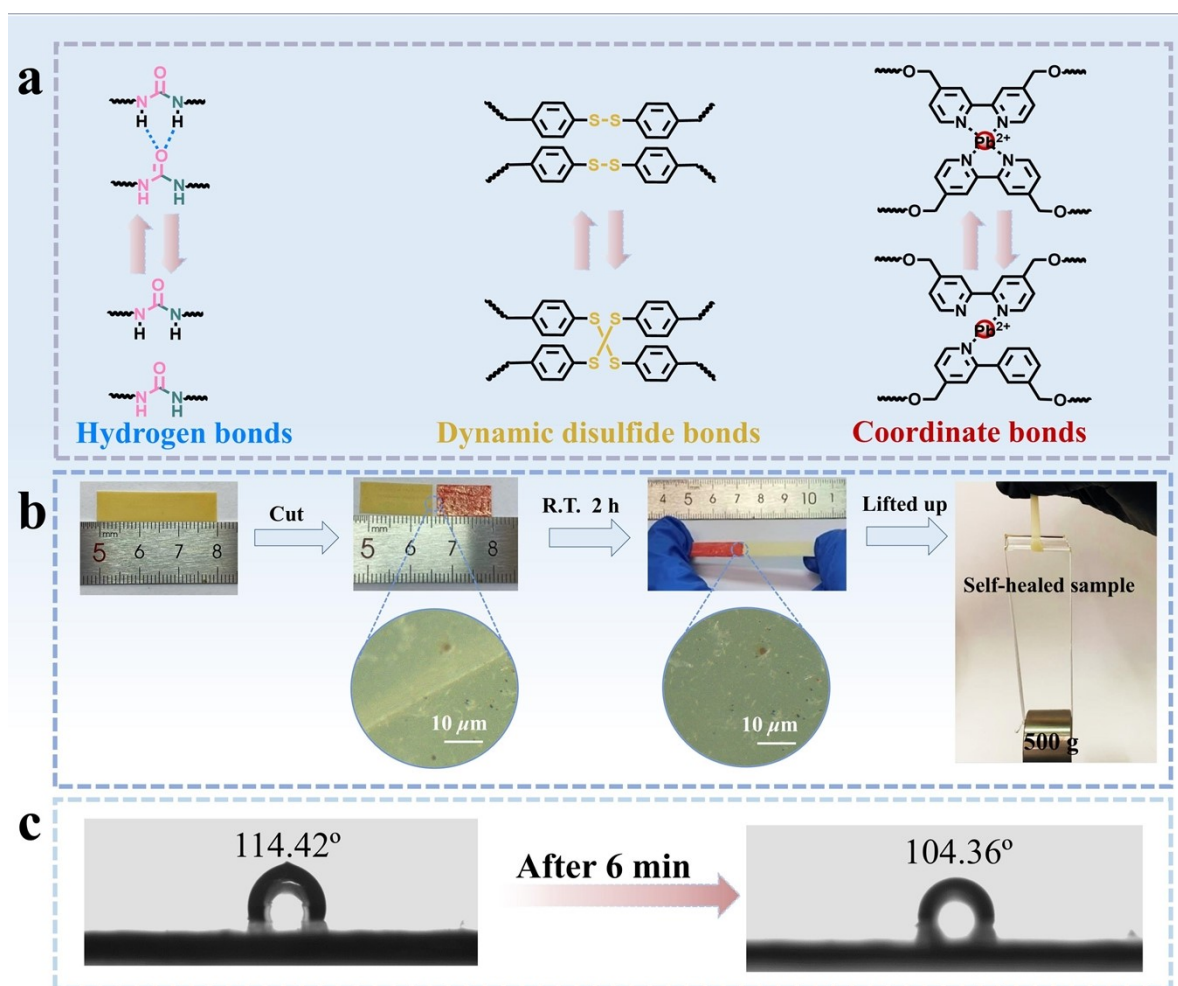


Fig. S2 (a) Schematic representation of the three molecular interactions in PAB. The breaking and recombination of dynamic non-covalent and covalent bonds endowed PAB with self-healing ability. (b) The dissected PAB samples could be self-healed in 2 h at room temperature, and the optical microscope showed that the crack disappeared, self-healed samples could be lifted up lastage. The red sample is stained with red ink. (c) Aqueous contact angle of PAB polymer before and after 6 min.

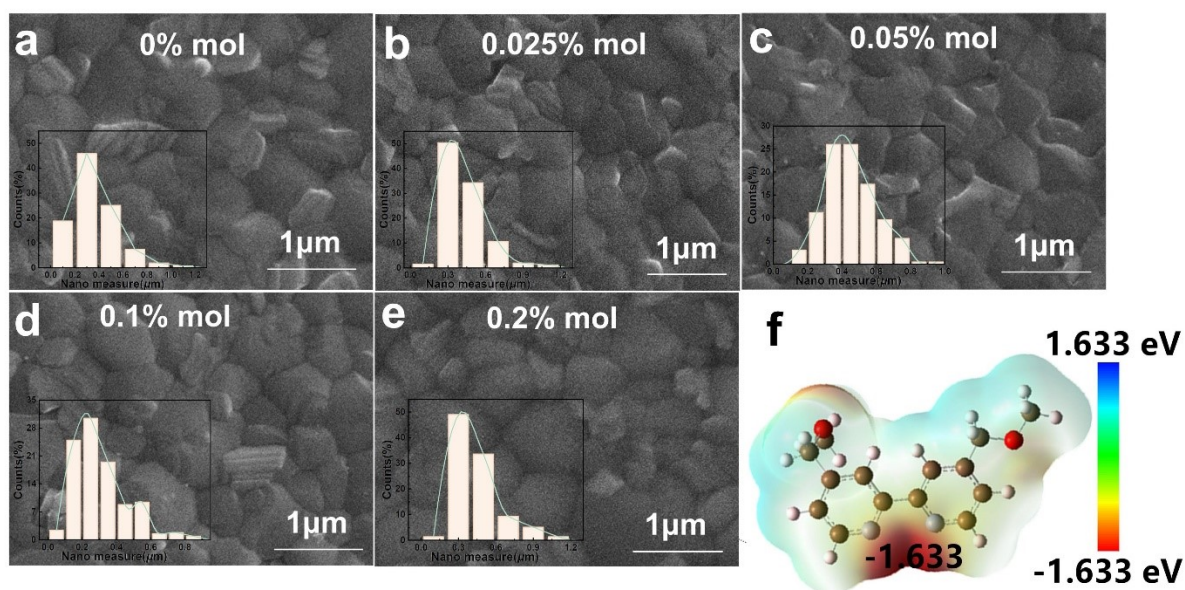


Fig. S3 (a)-(e) SEM images and grain size distribution histograms for perovskite films incorporating PAB at concentrations of 0% mol, 0.025% mol, 0.05% mol, 0.1% mol, and 0.2% mol. (f) The electrostatic potential of the bipyridine molecular structure calculated by density functional theory analysis.

After solvent removal of other layers

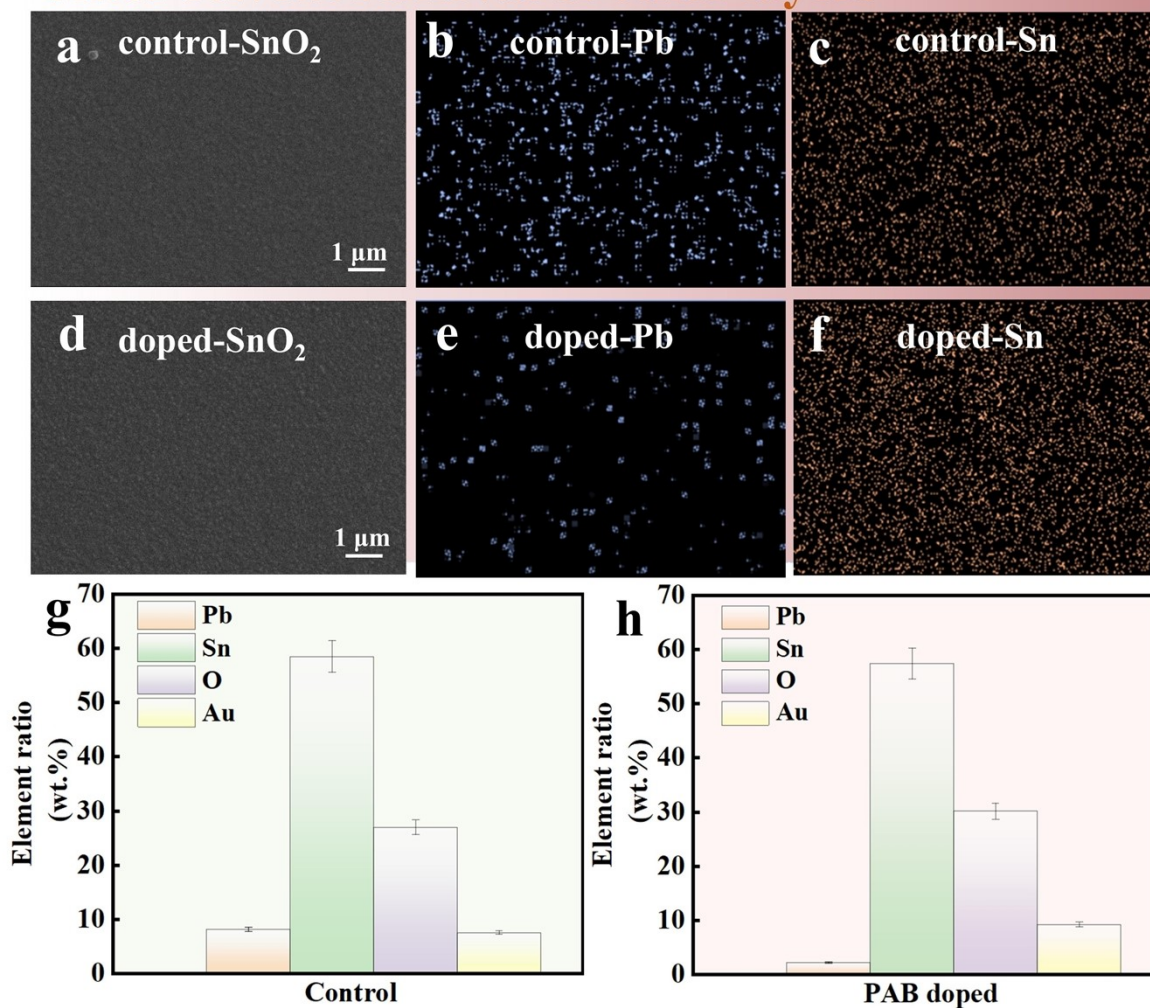


Fig. S4 SEM and mapping images of SnO₂ layer after dimethyl formamide (DMF) solvent removal of other layers. (a) and (d) SEM images of SnO₂ layer of doped and control. (b) and (e) distribution mapping of Pb element of doped and control. (c) and (f) distribution mapping of Sn element of doped and control. (g) and (h) Element ratio from EDS mapping images of control and PAB doped SnO₂ layer after dimethyl formamide (DMF) solvent removal of other layers.

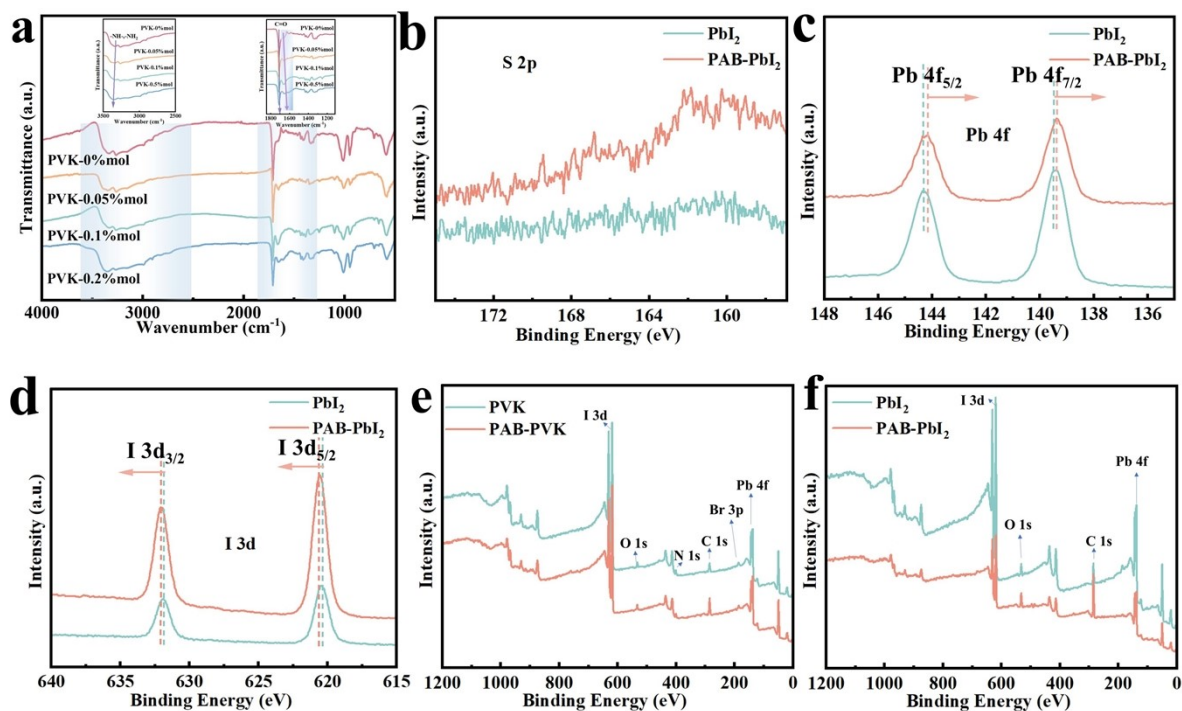


Fig. S5 (a) FTIR spectra of doped perovskite with polymer of different concentration, the absorption peaks of amide and carboxyl groups exhibited obvious redshift. (b)-(e) XPS diagram comparison of PAB doped and control PbI₂. (b) S, (c) Pb, (d) I, (e) Full XPS spectra of doped and undoped perovskite films. (f) Full XPS spectra of doped and control PbI₂.

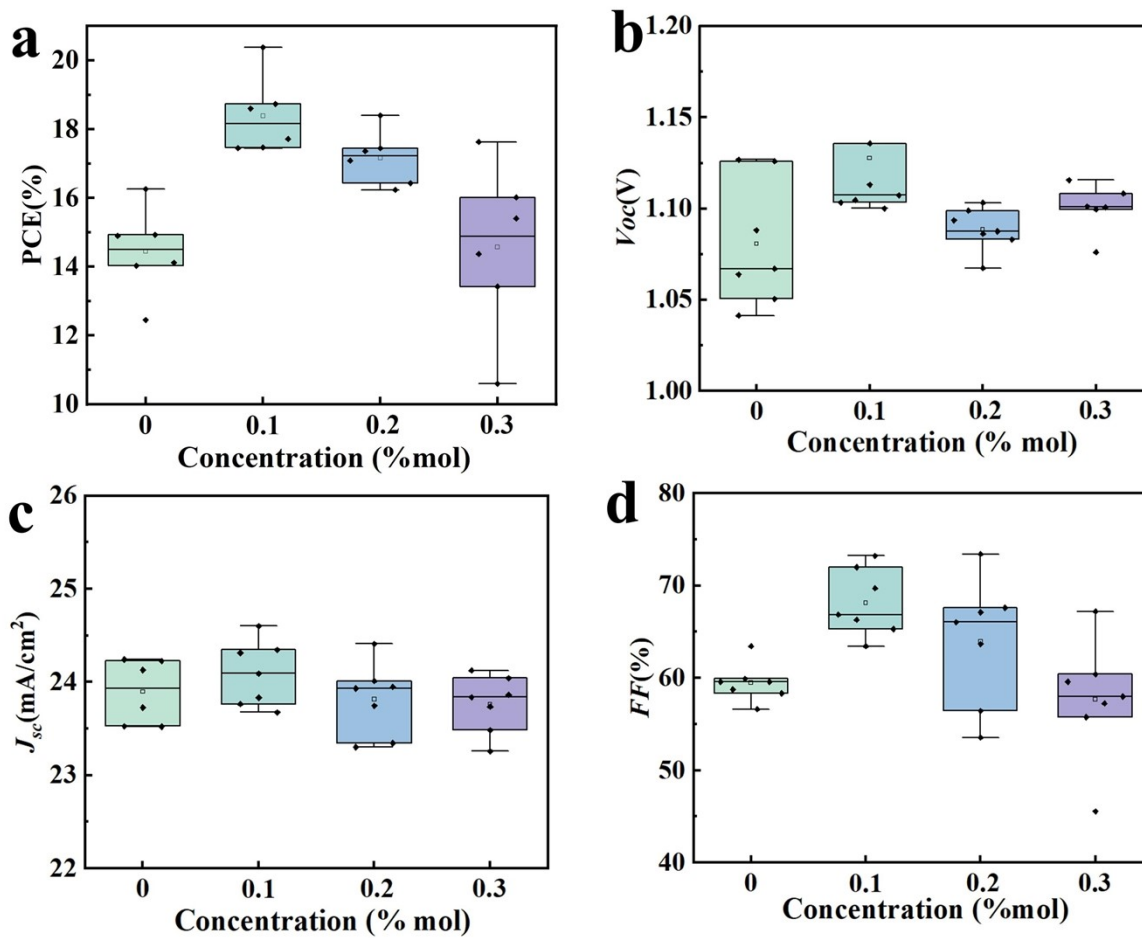


Fig. S6 (a) power conversion efficiency (PCE), (b) open-circuit voltage (V_{oc}), (c) the short-circuit current density (J_{sc}) and (d) fill factor (FF) of devices with different concentration of PAB. The performance of PSCs decreased with higher concentration. When the concentration of PAB of device was in the range of 0.1% mol with preferable performance of PSCs. Moreover, the concentration of PAB was further precisely controlled at 0.05% mol for the optimal performance of PSCs (Fig.4c).

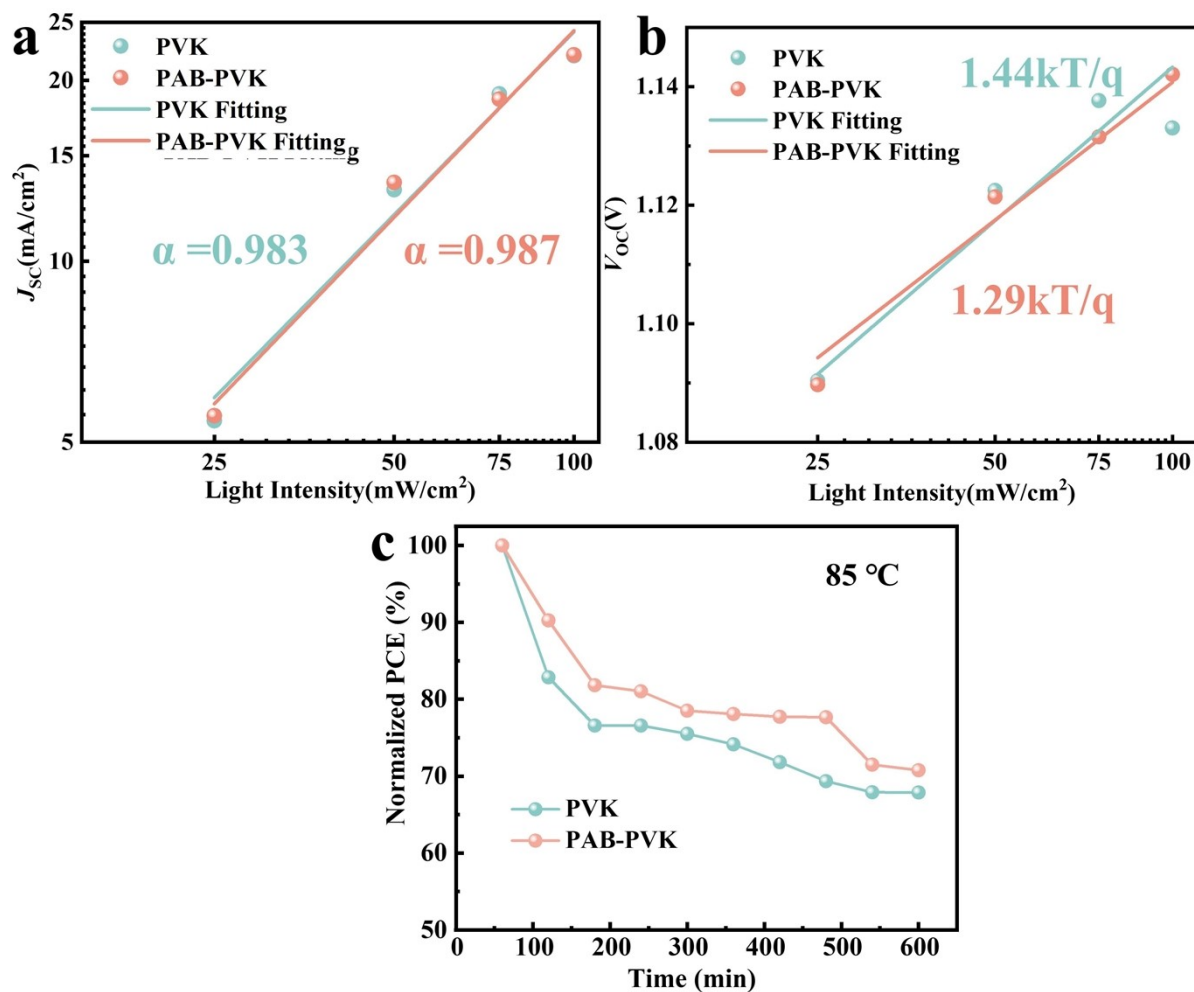
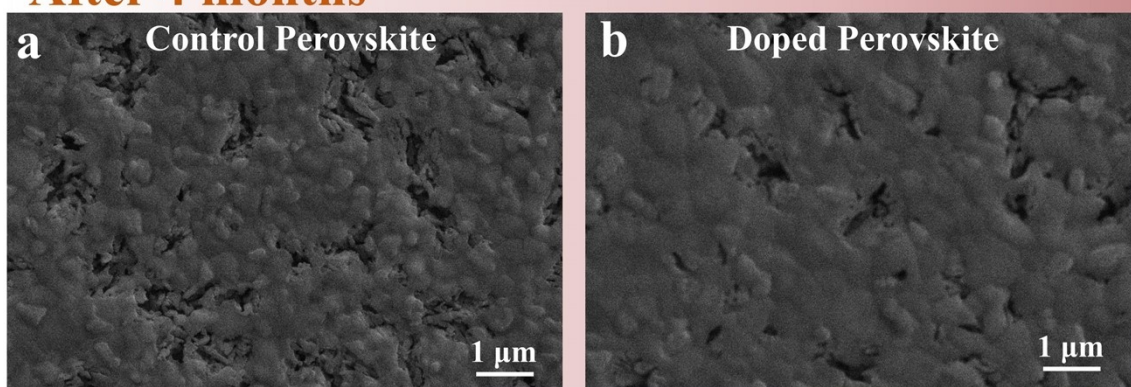


Fig. S7 (a) The relationship between the measured J_{sc} and light intensity of the control and PAB doped PSCs. (b) V_{oc} versus light intensity of the control and PAB doped PSCs. (c) Thermal stability tests of unencapsulated control and doped devices under 85 °C environments with a relative humidity level of 35%.

After 4 months



After 15 days

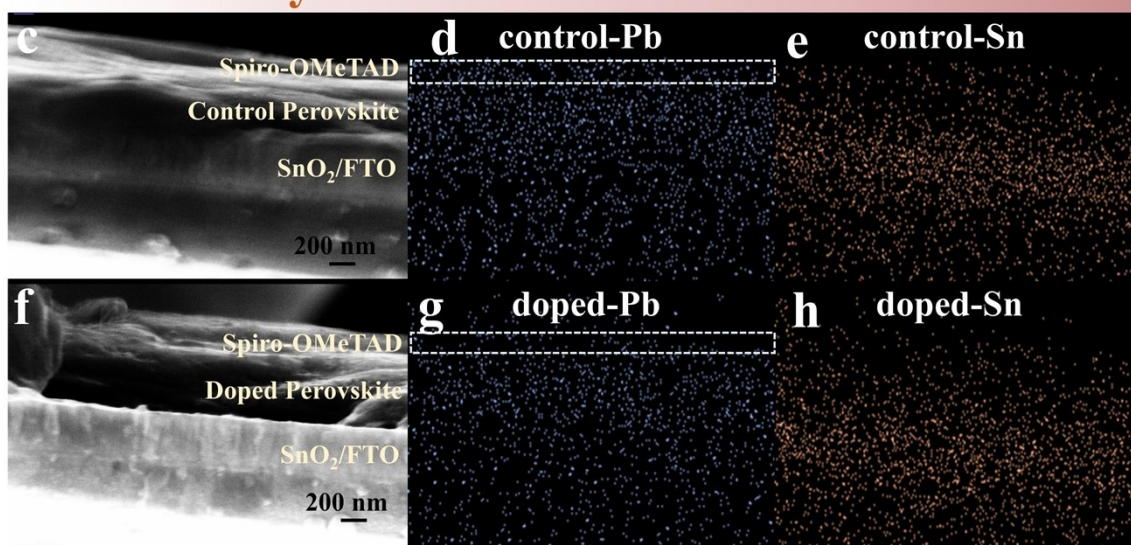


Fig. S8. The SEM images of the devices after storage in complete air atmosphere for 4 months and 15 days. (a) and (b) The surface SEM images of control and doped perovskite in complete air atmosphere for 4 months. (c) and (f) The cross-sectional SEM images and mapping of control and doped devices was further demonstrated the effect of enhancement stability after stockpiled in fully open-air conditions for 15 days. (d) and (g) distribution mapping of Pb element of doped and control devices for 15 days. (e) and (h) distribution mapping of Sn element of doped and control devices for 15 days.

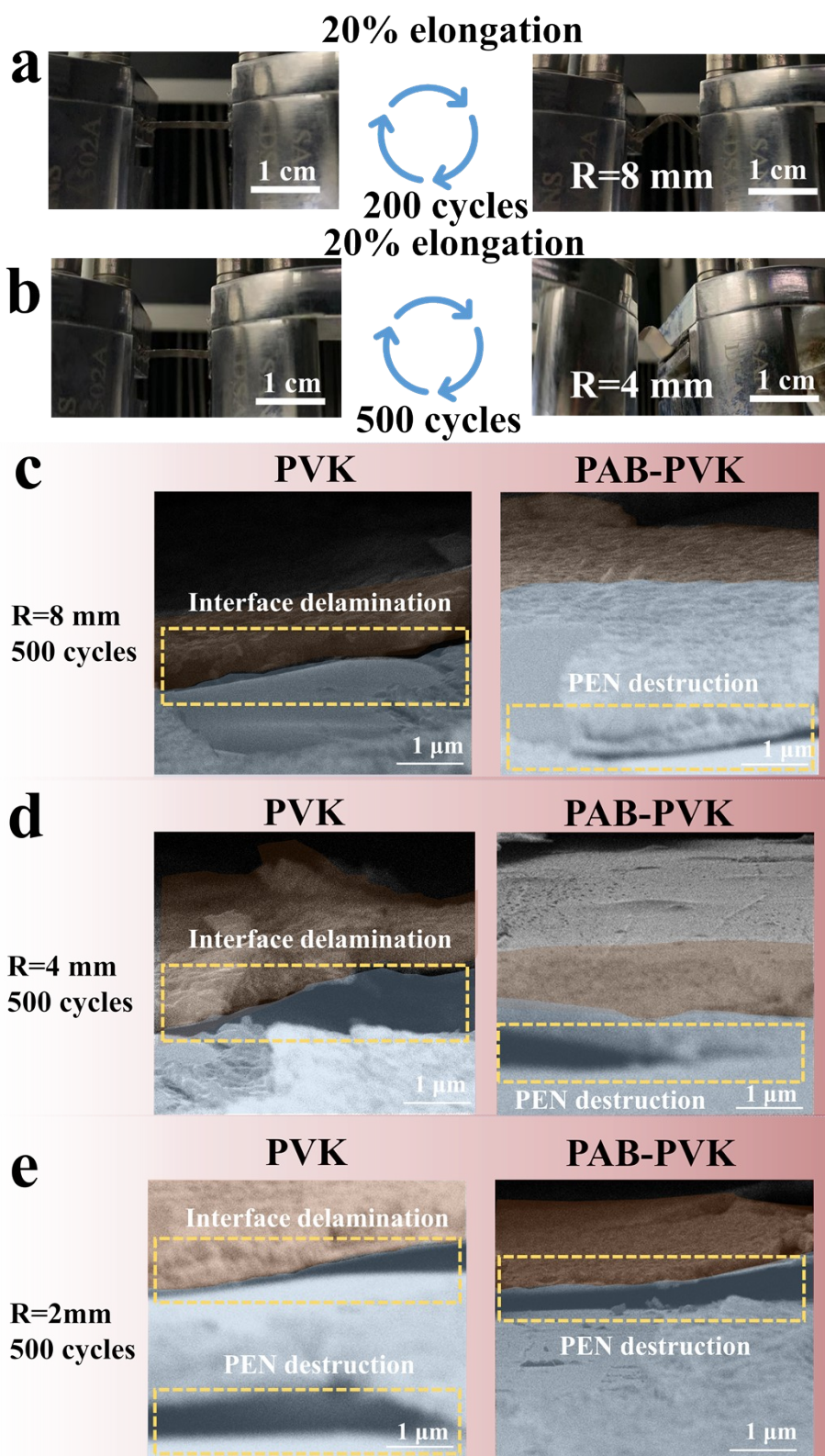


Fig. S9 Photographs and SEM images of cross-sections of the flexible PVK films with and without PAB after bending cycles under 20% strain; (a) Photographs of the flexible PVK films with PAB after 200 bending cycles under 20% strain ($R = 8$ mm). (b) Photographs of the flexible PVK films with PAB after 500 bending cycles under 20% strain ($R = 4$ mm). (c) SEM images of the flexible PVK films with and without PAB after 500 bending cycles under 20% strain ($R = 8$ mm). (d) SEM images of the flexible PVK films with and without PAB after 500 bending cycles under 20% strain ($R = 4$ mm). (e) SEM images of the flexible PVK films with and without PAB after 500 bending cycles under 20% strain ($R = 2$ mm).

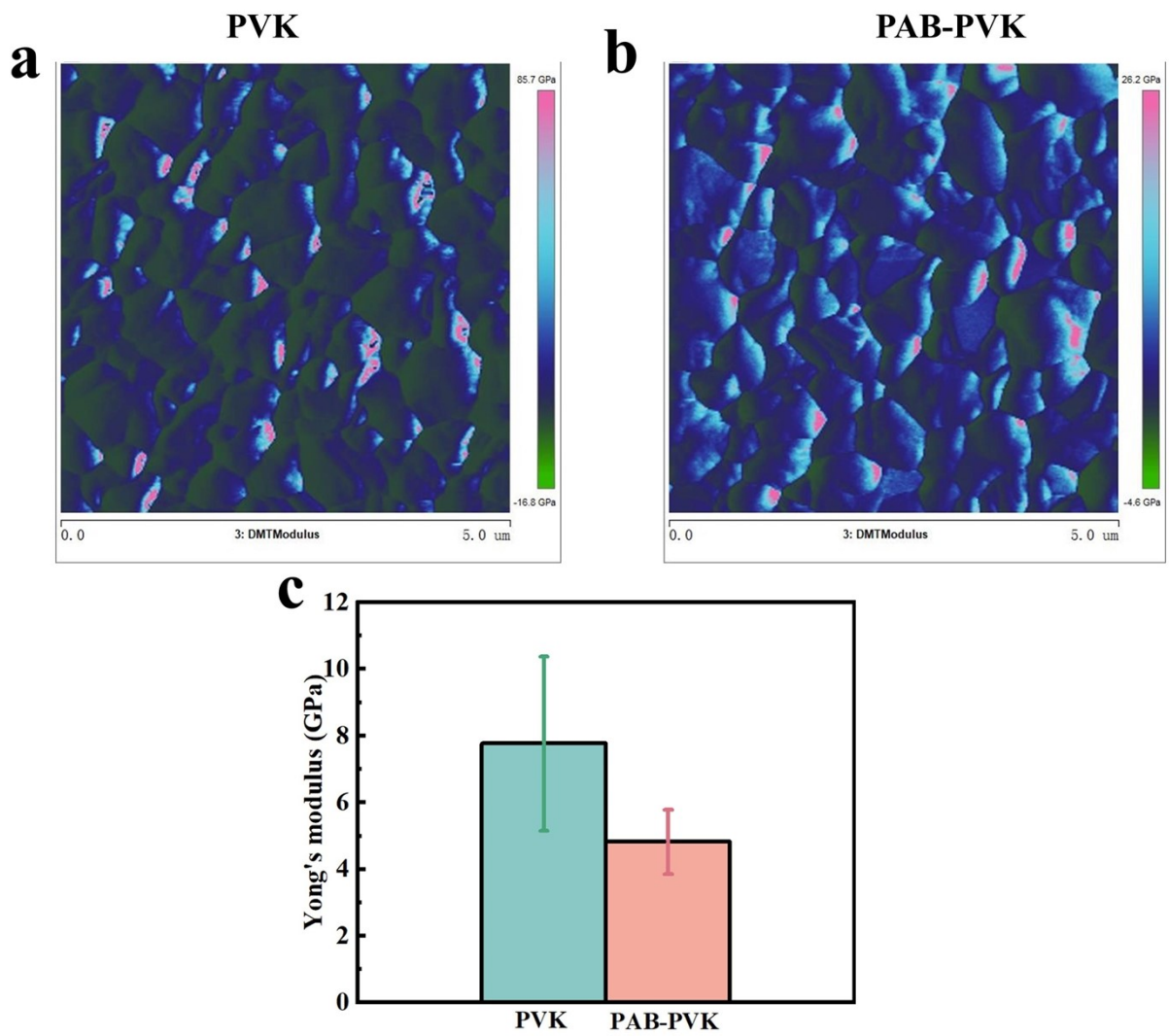


Fig. S10 (a)-(b) The Young's modulus of control film and doped film obtained from atomic force microscope measurements. (c) The Young's modulus of PAB polymer doped and control films.

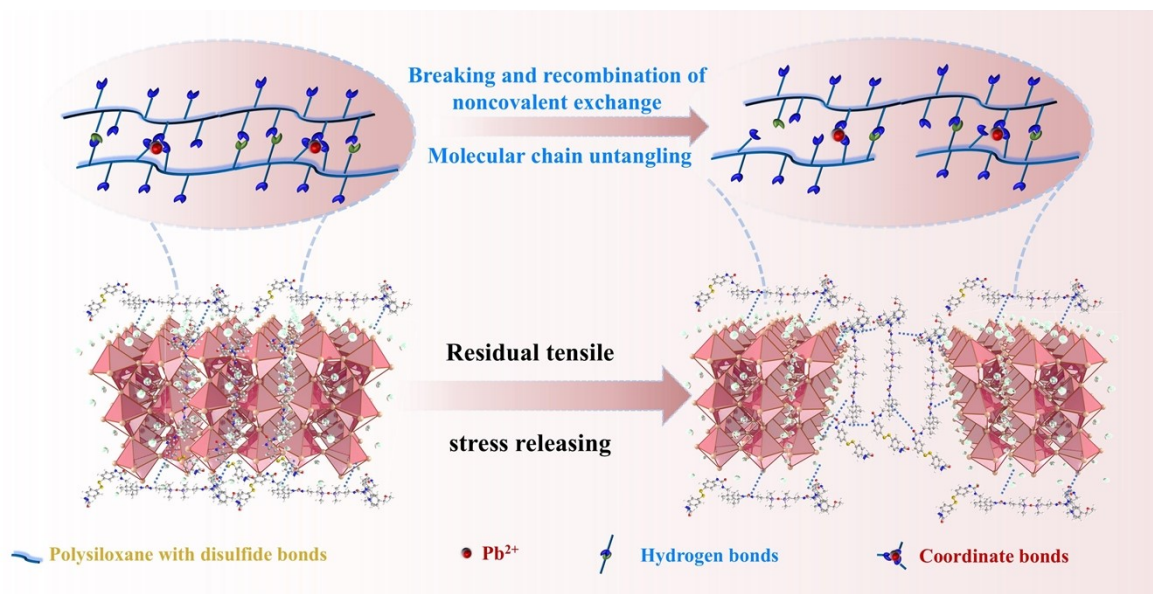


Fig. S11 Schematic diagram of residual tensile stress release.

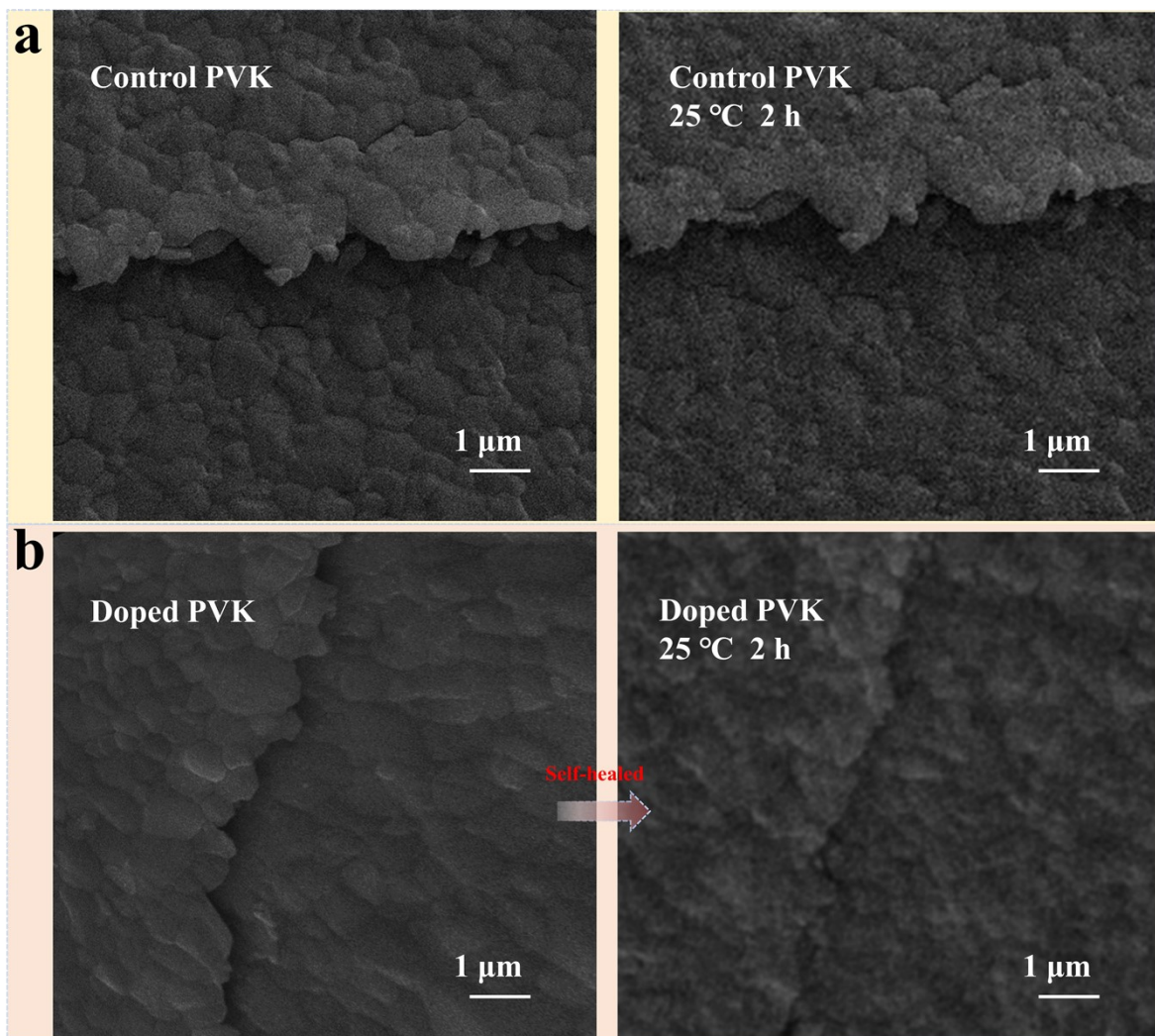


Fig. S12 The low-magnification SEM images of the control and doped perovskite films with mechanical cracks, comparing their appearance before and after self-recovery at 25 °C for 2 h.

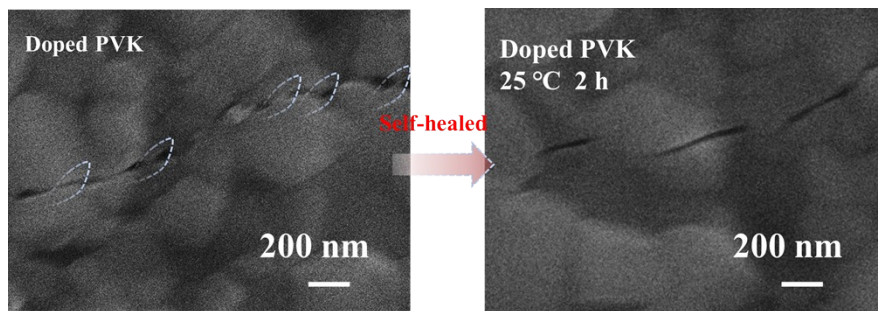


Fig. S13 The high-magnification SEM images show the control and doped perovskite films with mechanical cracks, highlighting their transformation before and after self-recovery at 25 °C for 2 h.

Table S1 Main particle size and corresponding percentage of perovskite doped at different PAB concentrations according to SEM from the Fig. S3a-e.

Sample	Main Nano measure (um)	Counts (%)
0% mol	~0.3	45.88%
0.025% mol	~0.3	45.88%
0.05% mol	~0.4	50.39%
0.1% mol	~0.3	52.04%
0.2% mol	~0.3	30.49%

Table S2 Device parameters of PSCs.

Device ^a		$V_{OC}(V)$	$J_{SC} (mA \cdot cm^{-2})$	$FF (%)$	$PCE (%)$
PVK	Reverse	1.17	21.35	76.75	19.12
	Forward	1.15	21.29	72.06	17.71
PAB-PVK (0.05% mol)	Reverse	1.17	22.19	81.18	21.02
	Forward	1.16	22.18	80.75	20.69

^a The effective area of the device measures 0.09 cm².

Table S3 Device parameters of PSCs.

Materials	R_s (Ω)	R_p (Ω)	C (F)
PVK	27.05	1.15	5.3767E-6
PAB- PVK (0.05% mol)	30.2	4.3	3.129E-7

Table S4 Relevant parameters for finite element simulation.¹

Materials	Thickness (μm)	Young's Modulus (GPa)	Density (g $\cdot\text{cm}^{-3}$)	Poisson's ratio
FTO	0.38	210	2.5	0.25
SnO ₂	0.03	5.414	6.95	0.29
PVK	0.624	7.77	4.1	0.33
PAB-PVK	0.624	4.82	4.1	0.33

Table S5 The summary of comprehensive device performance

Ref.	Preparation environment	Area (cm ²)	PCE (%)	Environmental Stability (T90)	Self-healing condition	Self-healing ability
This work	air	0.09	21.02	2000 h at 35% RH and 25 °C	R.T., 2 h	Dynamic covalent disulfide bonds, multiple hydrogen bonds and metal coordination bonds
2	N ₂	/	10.16	28 h at 50% RH and 25 °C	80 °C, 30 min	Dynamic disulfide bond
3	N ₂	/	17.42	3 h	100 °C, 1 h	Hydrogen bond
4	N ₂	/	19.03	2000 h at 50% RH and 25 °C	65 °C, 6 h	Disulfide bond
5	N ₂ and air	/	20.50	260 h at 85% RH and 85 °C	70 °C, 10 min	Hydrogen-bond
6	air	/	21.36	500 h at 50% RH and 25 °C	80 °C, 10 min	Disulfide bond
7	air and N ₂	/	20.46	12 h at 60-70% RH and 25 °C	60-70% RH, R.T. 4 h	Host-guest interaction
8	air	0.09	19.21	1440 h in an atmospheric environment	No	No
9	air	0.09	20.84	1000 h in an air environment	No	No
10	air	0.09	21.17	2400 h at 35% and RH 24 °C	No	No
11	N ₂	0.0784	18.5	300 s	No	No

Supplementary note 1

The trap state density (N_t) is determined by the following equation¹²:

$$N_t = \frac{2\varepsilon_r\varepsilon_0V_{TFL}}{qL^2}$$

Where ε_r is assigned to the relative dielectric constant of perovskite ($\varepsilon_r = 28.8$), ε_0 denotes the vacuum permittivity ($\varepsilon_0 = 8.854 \times 10^{-12} \text{ F}\cdot\text{m}^{-1}$), V_{TFL} corresponds to the onset voltage of the trap-filling limit. Additionally, q is the elementary charge ($q = 1.60 \times 10^{-19} \text{ C}$), L stands for the film thickness.

References

- 1 Z. H. Li, C. M. Jia, Z. Wan, J. Y. Xue, J. C. Cao, M. Zhang, C. Li, J. H. Shen, C. Zhang and Z. Li, *Nat. Commun.*, 2023, **14**, 6451.
- 2 Q. Y. Zhang, J. L. Duan, Q. Y. Guo, J. S. Zhang, D. D. Zheng, F. X. Yi, X. Y. Yang, Y. Y. Duan and Q. W. Tang, *Angew. Chem. Int. Ed.*, 2022, **61**, e202116632.
- 3 B. P. Finkenauer, Y. Gao, X. K. Wang, Y. Tian, Z. T. Wei, C. H. Zhu, D. J. Rokke, L. R. Jin, L. Meng, Y. Yang, L. B. Huang, K. J. Zhao and L. T. Dou, *Cell Rep. Phys. Sci.*, 2021, **2**, 100320.
- 4 J. Yang, W. P. Sheng, X. Li, Y. Zhong, Y. Su, L. C. Tan and Y. W. Chen, *Adv. Funct. Mater.*, 2023, **33**, 2214984.
- 5 C. D. Ge, X. T. Liu, Z. Q. Yang, H. M. Li, W. W. Niu, X. K. Liu and Q. F. Dong, *Angew. Chem. Int. Ed.*, 2022, **61**, e202116602.
- 6 T. Zheng, Q. Zhou, T. Yang, Y. Zhao, B. Fan, J. Bo, L. S. Fan and R. F. Peng, *Carbon*, 2022, **196**, 213-219.
- 7 Z. C. Yang, Y. Jiang, D. D. Xu, Z. Wang, X. S. Gao, X. B. Lu, G. F. Zhou, J. M. Liu and J. W. Gao, *J. Mater. Chem. A*, 2022, **10**, 22445-22452.
- 8 J. Y. Liu, X. He, X. Li and Y. Li, *New J. Chem.*, 2022, **46**, 9841-9850.
- 9 G. Y. Zeng, G. Y. Liu and X. Li, *ACS Sustainable Chem. Eng.*, 2023, **11**, 7664-7672.
- 10 G. Y. Liu, G. Y. Zeng, Z. Q. Ren, J. Y. Liu and X. Li, *Sol. RRL*, 2024, **8**, 2400043.
- 11 R. Pappenberger, A. Diercks, J. Petry, S. Moghadamzadeh, P. Fassel and U. W. Paetzold, *Adv. Funct. Mater.*, 2024, **34**, 2311424.
- 12 T. Y. Xue, B. J. Fan, K. J. Jiang, Q. Guo, X. T. Hu, M. Su, E. R. Zhou and Y. L. Song, *Energy Environ. Sci.*, 2024, **17**, 2621-2630.